Coupling Effect of Particle Deposition Inside and Outside Holes on Film Cooling Performance on the Leading Edge of the Blade

G. Li[†], G. Zhang, H. He, C. Zhao, Z. Zhao and W. Zhang

School of Aero-engine, Shenyang Aerospace University, Shenyang, Liaoning, 110136, China

†*Corresponding Author Email: liguangchao@stu.sau.edu.cn*

ABSTRACT

A numerical investigation of the particle deposition characteristics inside film holes and on the blade was conducted using an improved particle deposition model and dynamic grid updating. The computation model was numerically simulated using Reynolds-Averaged Navier-Stokes (RANS) equations with second-order spatial accuracy and the SST k-ω turbulence model, combined User Defined Function (UDF) in FLUENT 2021R1. The influence of the deposition morphology on film effectiveness was analyzed. The results revealed that a conical deposition in the exit region inside the film holes enhanced the separation of the coolant ejected from the film holes at a low coolant mass flux ratio (MFR). Increasing the MFR inhibited deposition, and the enhanced particle detachment significantly reduced particle deposition inside the film holes. Deposition downstream of the film holes significantly affected the cooling performance. Strip deposition on both sides of the region covered by the coolant limited the spanwise diffusion of the coolant. Compared to the non-deposition case, The surface-averaged film effectiveness was lower after deposition at MFRs of 0.1%-0.5% and slightly higher at MFRs of 0.6%. The most significant reduction in the surface-averaged film effectiveness after deposition was 34.9% at an MFR of 0.3%.

1. INTRODUCTION

When an aircraft takes off, cruises, or lands in an environment with sand and fly ash, the particles entering the engine are deposited on the blade, changing its aerodynamic profile due to high-temperature gas. Particle deposition significantly reduces the engine's cooling performance, potentially causing the failure of the cooling system (Kim et al., 1993; Lewis et al., 2010; Dunn, 2012).

Several studies were recently conducted on particle deposition in engines. Jensen et al. (2004) simulated particle deposition during four hours after 10000 hours of operation in a turbine-accelerated deposition facility (TADF). Crosby et al. (2008) utilized the same device to study the relationship between gas temperature and particle deposition. The result showed that the rate of particle deposition on the blade increased significantly with the gas temperature. Lundgreen et al. (2016) investigated the effect of the turbine entry temperature on turbine blade deposition. The deposition on the pressure surface increased with the temperature, and the deposition was concentrated at the blade's leading edge. Barker et al.

(2012) and Ai and Fletcher (2012) investigated the effect of particle size on the deposition process. Small particles followed the main flow and had less influence on the blade, whereas large particles had a greater impact on the blade. Lawson and Thole (2011) analyzed the effect of the Stokes number and Tsp on particle deposition and deposition characteristics for molten wax and real particles. Zhang et al. (2020) assessed the influence of the attack angle on deposition using liquid wax instead of molten microparticles. Bons et al. (2017) examined particle deposition using an improved critical velocity model (Brach & Dunn, 1992; El-Batsh & Haselbacher, 2002). As the Stokes number increased, the adhesion rate increased and decreased rapidly. Hao et al. (2023) used an unsteady simulation method to study particle deposition characteristics for different rotational speeds of the blade and particle diameters.

Numerous scholars have found that the effect of cooling jets in film holes cannot be ignored. Bonilla et al. (2012, 2013) investigated the deposition characteristics of a turbine vane. They found that the coolant flow ejected from the film holes substantially reduced particle deposition downstream of the film holes. Albert and

Bogard (2013) observed thicker deposits on the downstream wall between coolant jets in low-temperature wax deposition experiments. Ai et al. (2011) assessed the deposition distribution on flat plates near film cooling holes using the El-Batsh model. They discovered that increasing the diameter of the film hole decreased the particle deposition rate. Borello et al. (2014) found that the cooling jet removed fluid close to the wall and reduced the blade temperature, affecting particle deposition. Wang et al. (2016) investigated the deposition and blockage of film holes at the leading edge of the blade using a numerical method. The results showed that the probability of particle deposition in the holes was lower for small than large particles at low blowing ratios. Kistenmacher et al. (2013) experimentally investigated particle deposition in holes with grooves and observed that fewer particles were deposited in the optimum groove design.

Although many studies investigated the deposition characteristics on blades and in film holes, few have focused on the effect of particle deposition on the cooling performance. Sundaram et al. (2008) experimentally analyzed the effect of particles in different deposition regions on film cooling performance. Bons (2010) found that the deposition structure on the blades altered the aerodynamic profile and changed the flow direction. Albert and Bogard (2012) and Lawson et al. (2012) discussed the influence of the location and thickness of particle deposition on film effectiveness. The results showed that the coolant affected particle deposition, and the deposition morphology influenced film effectiveness. Yang et al. (2021a) investigated particle deposition during the early stage in a blade passage with minor grid deformation. They found that slight deposition improved film effectiveness. The effect of coolant injection from the casing and endwall in the turbine component on cooling performance cannot be ignored. (Abbasi & Gholamalipour, 2020; 2021). Lawson and Thole (2010) found that endwall cooling is highly sensitive to deposition. Excess deposition could lead to reduced cooling effectiveness and possibly turbine component failure.

The leading edge of the blade endures severe aerodynamic heating, therefore, the leading edge and coolant inject to the stagnation region have high importance. (Vali & Abbasi, 2022, 2024) Although some studies investigated the deposition of the blade's leading edge, most focused on the particle deposition characteristics and distribution. However, the influence of the deposition structure on the flow field has not been analyzed. Most studies on the influence of particle deposition on film effectiveness were experimental studies (Ai et al. 2011; Zhang et al. 2020) that focused on the deposition characteristics, whereas the reasons for the influence were not examined in-depth. During the growth of deposition, deposition structure inside the film holes and on the blade surface has different effects on the flow field. In previous studies, only the influence of the deposition structure on the blade surface was considered, and there were few studies of the coupling effect of the deposition structure in the film hole and the blade surface. This paper considers the interaction between the particle deposition structure and the flow field and analyzes the coupling effects of the deposition inside film holes and on

the blade on the film cooling performance. The focus is to investigate the influences of the deposition structure on the flow field inside the film hole and on the blade surface. An improved composite deposition model and dynamic mesh updating method are used to examine the coupling effect of deposition morphology on film cooling performance for different mass flux ratios (MFRs).

2. COMPUTATION MODEL AND BOUNDARY CONDITIONS

Figure 1 shows the computational model of the three-dimensional cascade channel of the turbine in an aero-engine. The inlet flow angle is 49.5°, and the outlet flow angle is 27.3°. The chord length of the blade is 143.3 mm, and the pitch of the cascade is 109.7mm. One row of film holes with diameters of 1.72 mm is located at the blade's leading edge. The inclination angle of the film holes to the surface is 34°, and the orientation angle is 90°.

Numerical simulations were conducted using the commercial computational fluid dynamics software FLUENT 2021R1 with the discrete phase model (DPM). The boundary conditions consisted of a pressure inlet at the entrance and a pressure outlet at the exit of the cascade channel. The coolant flow rate was based on the coolant's MFR. The side wall of the cascade channel had periodic boundary conditions, and the other walls had adiabatic conditions. The hot and cold fluids were compressible ideal fluids. The boundary conditions are listed in Table 1.
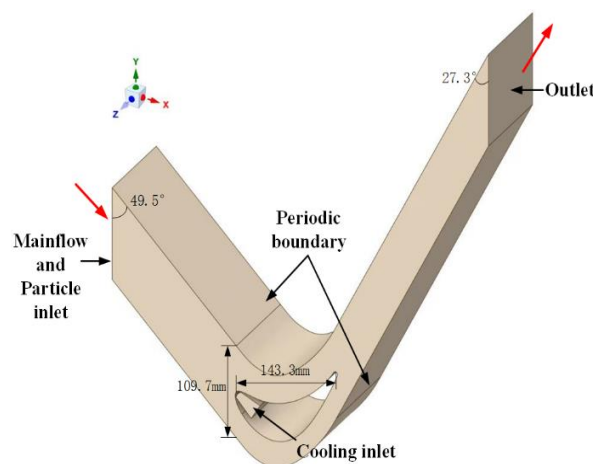

Fig. 1 Computational domain

Table 1 Computational boundary conditions

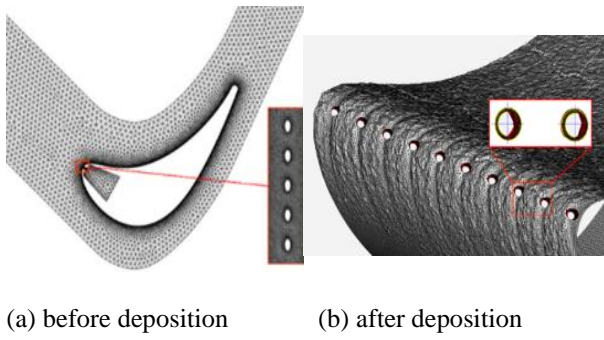| Parameters	Value
Inlet total pressure $P_{t,in}$	1800 kPa
Inlet total temperature $T_{t,in}$	1650 K
Outlet static pressure $P_{s,out}$	1000 kPa
Drop pressure ratio	1.8
Coolant inlet temperature $T_{c,in}$	800 K
Turbulence intensity Tu	2%

(a) before deposition   (b) after deposition

Fig. 2 Mesh view

Table 2 Material properties of incident particles

Parameter	Value
Density ρ_p	2320 kg/m^3
Specific heat C_p	984 J/(kg·k)
Thermal conductivity k	0.5 W/(m·k)
Minimum diameter d_{min}	1 μm
Maximum diameter d_{max}	20 μm
Average diameter d_{ave}	13.4 μm

As shown in Fig. 2(a), the computational domain consisted of a tetrahedral mesh created in the Fluent meshing software. The mesh was refined near the blade walls and film holes. The number of grids was 3.7 million after grid-independence analysis. The grid on the surface before and after particle deposition is shown in Fig. 2(b).

The DPM tracked the particles released uniformly from the main flow inlet after the convergence of the continuous phase. One-way coupling was adopted, and the diameter had a logarithm Rosin-Rammler distribution. The discrete random walk model was used to model the turbulent dispersion of particles. Each particle occupied one grid, and 100 surface incidences were simulated. The particles had the same temperature and moved at the same velocity as the fluid. The material properties of the incident particles are listed in Table 2

3. MATHEMATICAL MODEL

The particles were assumed to be hard spheres and simplified to points at the sphere's center. The Reynolds-averaged Navier-Stokes (N-S) equations and the SST k-ω turbulence model were used to solve the velocity and thermal fields of the continuous phase using the Euler method. The SST k-ω model combines the advantages of the k-ε model and k-ω model, providing accurate and reliable turbulence prediction results in the boundary and free layers. The SST k-ω model generates a reliable blade flow field (Lee et al. 2018; Liu et al. 2018). The trajectory of the particles in the flow was tracked using the Lagrangian method to obtain the particles' temperature and velocity parameters.

A steady simulation was used, and the particles were released uniformly from the main flow inlet after the convergence of the continuous phase. The particle behavior after impacting the wall (adhesion, detachment, or deposition) was determined using a user-defined

function (UDF). Subsequently, dynamic mesh updating was implemented to alter the shape of the surface mesh based on the deposition distribution, followed by recomputing of the flow field. The process was repeated to analyze changes in deposition morphology and the influence of the deposition structure on the flow field.

3.1 Particle Tracking

The model considers the effect of the drag force (F_d), Saffman lift (F_s), and thermophoretic force (F_t) on the particle transport. The motion equations for the particles in the fluid are as follows:

$$m_p \frac{du_p}{dt} = F_d + F_s + F_t \tag{1}$$

where m_p is the mass and u_p is the velocity of the particle.

$$F_d = \frac{1}{2}\rho\left(u - u_p\right)^2 A_{cp}C_d \tag{2}$$

$$F_s = 1.615\mu u_p{}^2\sqrt{\frac{k_r}{v}}\left(u - u_p\right) \tag{3}$$

$$F_t = -D_{T,p}\frac{1}{T}\nabla T \tag{4}$$

where A_{cp} is the particle's front area, k_r is the local velocity gradient, and u and u_p are, respectively, the velocities of the fluid and particles. μ is the dynamic viscosity of the fluid, v is the fluid's kinematic viscosity, ρ is the fluid density; C_d is the drag coefficient of the particle, and $D_{T,p}$ is the thermophoretic coefficient.

The temperature of the particles is calculated as follows:

$$m_p c_p \frac{dT_p}{dt} = h_c A_p\left(T_f - T_p\right) \tag{5}$$

where A_p is the surface area of the particle, c_p is the specific heat capacity of the particle, and T_f and T_p are the temperatures of the fluid and the particle, respectively. h_c is the surface heat transfer coefficient between the fluid and the particle derived from the Ranz-Marshall empirical correlation.

3.2 Particle Deposition Model

The flow field and particle properties influence particle deposition. Particle-wall interactions include adhesion and detachment. The former is influenced by the particle temperature and velocity, and the latter is affected by the adhesion friction force and the shear force. The proposed composite deposition model is advantageous because it considers the influences of viscosity and velocity.

This model consists of the critical velocity model (El-Batsh & Haselbacher, 2002) and the critical viscosity model (Sreedharan & Tafti, 2011). It was used to calculate the adhesion probability as follows:

$$P_s\left(T_p\right) = \frac{\mu_{crit}V_{cr}}{\mu_{T_p}V_n} \tag{6}$$

Table 3 Categories of adhesion probability

No.	T_p	V_n	P_s
1	$T_p \geq T_{crit}$	$V_n < V_{cr}$	1
2	$T_p \geq T_{crit}$	$V_n \geq V_{cr}$	V_{cr}/V_n
3	$T_p < T_{crit}$	$V_n < V_{cr}$	μ_{crit}/μ_{Tp}
4	$T_p < T_{crit}$	$V_n \geq V_{cr}$	$\mu_{crit}V_{cr}/(\mu_{Tp}V_n)$

where V_n is the normal particle velocity, V_{cr} is the critical impact velocity, μ_{Tp} is the kinetic viscosity at the current temperature, and μ_{crit} is the kinetic viscosity at the critical temperature.

The critical impact velocity of the particle (V_{cr}) is defined as follows:

$$V_{cr} = \left(\frac{2E}{D_p} \right)^{\frac{10}{7}} \tag{7}$$

$$E = 0.51 \left[\frac{5\pi^2 \left(k_1 + k_2 \right)}{4\rho_p^{\frac{3}{2}}} \right]^{\frac{2}{5}} \tag{8}$$

$$k_1 = \frac{1 - v_s^2}{\pi E_s} \tag{9}$$

$$k_2 = \frac{1 - v_p^2}{\pi E_p} \tag{10}$$

where E is the composite Young's modulus, which depends on k_1 and k_2. E_s and E_p are Young's moduli of the wall and the particle, respectively. v_s and v_p are the Poisson's ratios of the wall and the particle, respectively.

The relationship between particle viscosity and temperature (Senior & Srinivasachar, 1995) is expressed as follows:

$$\ln \left(\frac{\mu}{T_p} \right) = A + \frac{10^3 B}{T_p} \tag{11}$$

where T_p is the particle temperature. It is assumed that A and B are -11.31 and 15.96, respectively, according to the particle composition.

The experimental data indicate that the critical temperature of most particles in the turbine is 1478 K. This study assumes a critical temperature of 1480 K. The categories for the particle adhesion probability are listed in Table 3.

The shear force may detach particles deposited on the wall surface. The balance between the adhesion and detachment forces determines the final deposition amount. According to the critical momentum theory, a comparison of the shear velocity and critical shear velocity at the wall can be used to determine whether particle detachment occurs. The critical shear velocity and shear velocity are expressed as:

$$u_{\tau c}^2 = \frac{C_u W_A}{\rho D_p} \left(\frac{3\pi W_A}{2 D_p K_c} \right)^{\frac{1}{3}} \tag{12}$$

$$u_{\tau} = \sqrt{\frac{\tau_w}{\rho}} \tag{13}$$

where W_A is the adhesion constant. The composite Young's modulus K_c is expressed as:

$$K_c = \frac{4}{3} \left(\frac{1 - v_s^2}{E_S} + \frac{1 - v_p^2}{E_p} \right)^{-1} \tag{14}$$

3.3 Dynamic Mesh Methods

A dynamic mesh technique was utilized to determine the changes in the deposition morphology. The flow field was updated after deposition to calculate the particles' trajectories. This process was performed 100 times to simulate changes in the deposition morphology. The normal reconstruction method was used to adjust the grid after particle deposition. The normal displacement of the mass center of each grid was calculated close to the wall. The displacement was obtained using the following expression:

$$\Delta H = \frac{q_t}{\rho_p S_i} f_{ni} \tag{15}$$

where $\triangle H$ is the node displacement. q_t is the mass deposited in the grid cells; ρ_p is the particle density. S_i is the area of the cell face close to the boundary. f_{ni} is the normal vector of the grid cell face. Smooth diffusion was used for dynamic mesh deformation to update the wall profile after particle deposition and perform mesh reconstruction. A large diffusion factor was chosen to prevent tearing and breaking during mesh deformation.

The elastic modulus and Poisson's ratio of the wall depend on whether the particles impact the wall or are deposited. The particle diameter and deposition thickness were compared to determine this.

3.4 Definition of Parameters

The following equations were used to determine the impact rate P_i, adhesion rate P_t, deposition rate P_d, and detachment rate P_l to characterize the particle impact and deposition:

$$P_i = \frac{m_i}{m_{total}} \tag{16}$$

$$P_t = \frac{m_t}{m_i} \tag{17}$$

$$P_d = \frac{m_d}{m_{total}} \tag{18}$$

$$P_l = \frac{m_t - m_d}{m_t} \tag{19}$$

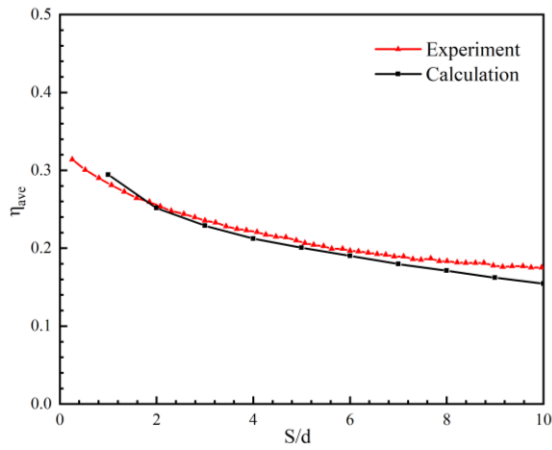**Fig. 3 Validation of SST k-ω model**

Fig. 4 Validation of deposition model

where m_i is the mass of the particles impacting the blade; m_{total} is the total mass of the injected particles; m_t is the mass of the particles adhering to the blade; m_d is the mass of the particles deposited on the blade. The impact rate P_i was used to reflect the potential of particles impacting the blade. The adhesion rate P_t represented the potential of particles adhering to the blade surface after the impact. The deposition rate P_d denoted the probability of particles being deposited on the blade surface after adherence and detachment. The detachment rate P_l reflected the potential of particles being detached from the blade after adhering.

The film effectiveness is defined as:

$$\eta = \frac{T_g - T_{aw}}{T_g - T_c} \tag{20}$$

The dimensionless temperature is defined as:

$$\theta = \frac{T_g - T_a}{T_g - T_c} \tag{21}$$

where T_g is the main flow temperature; T_{aw} is the adiabatic wall temperature; T_c is the coolant temperature; T_a is the temperature of the main flow and coolant.

The film hole exit was located at the leading-edge stagnation line, where the local velocity of the main flow was zero. Thus, the MFR instead of the local blowing ratio was used to determine the working conditions. It is defined as:

$$MFR = \frac{m_c}{m_g} \tag{22}$$

where m_c is the coolant mass flow rate through the film holes on the leading edge, and m_g is the mass flow rate of the mainstream flow through one passage of the cascade.

3.5 Validation of Computational Method

The numerical simulation results were compared with the experimental results to verify the accuracy of the computational method. However, there is a lack of appropriate experimental data about the effect of deposition structure. Therefore, the numerical results of
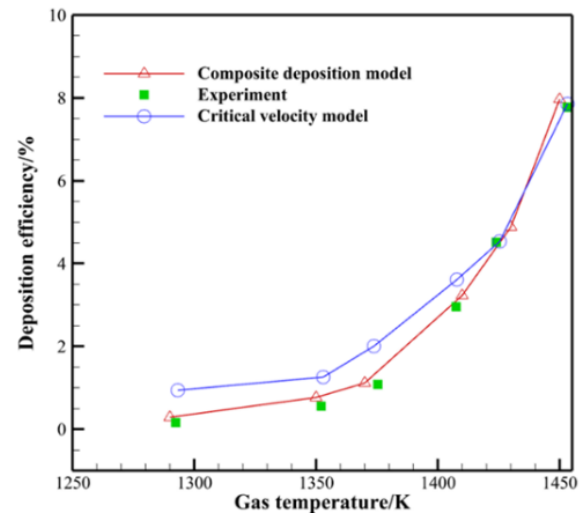
spanwise averaged film effectiveness are verified with the experimental results by Maikell et al. (2011) with the same location of film holes on the blade. As shown in Fig .3, the calculated data matches well with the experimental data through comparison of the spanwise averaged film effectiveness, indicating that the SST k-ω model has good predictive performance for the flow field inside the turbine cascade.

As shown in Fig .4, the composite deposition model has a better agreement with the experimental data of Ai and Fletcher (2012) than the critical velocity model. This result indicates that the proposed model can accurately calculate the deposition characteristics.

4. RESULTS AND DISCUSSION

4.1 Effect of Film Cooling Jet On Particle Deposition

The effect of the MFR on particle deposition was analyzed in the range of 0.1%-0.6%. The deposition morphology inside the film holes is shown in Fig 5(a). A conical deposition structure covering about 50% of the hole width is observed at an MFR of 0.1%. A small amount of deposition occurs near the film hole exit at MFRs of 0.2%-0.3%. Most of the particles entering the film holes are blown away due to the higher coolant velocity, and only a few particles are deposited inside the film holes at MFRs of 0.4%-0.6%. Figure 5(b) illustrates the particle deposition mass inside the film holes at different MFRs. The deposition mass decreases considerably with an increase in the MFR. A negligible deposition mass occurs inside the film holes at MFRs of 0.4%-0.6%. The result implies that deposition is more likely during takeoff because less coolant flows through the film holes, and particles enter the engine due to a dusty environment.

Particle deposition occurs primarily at the leading edge and the pressure surface of the blade as shown in Fig. 6. The deposition characteristics are consistent with the experimental results of Zhang et al. (2020) and El-Batsh et al. (2011). The particles are deposited on the wall not covered by the coolant. The deposition occurs in strips on both sides of the region covered with the film due to the
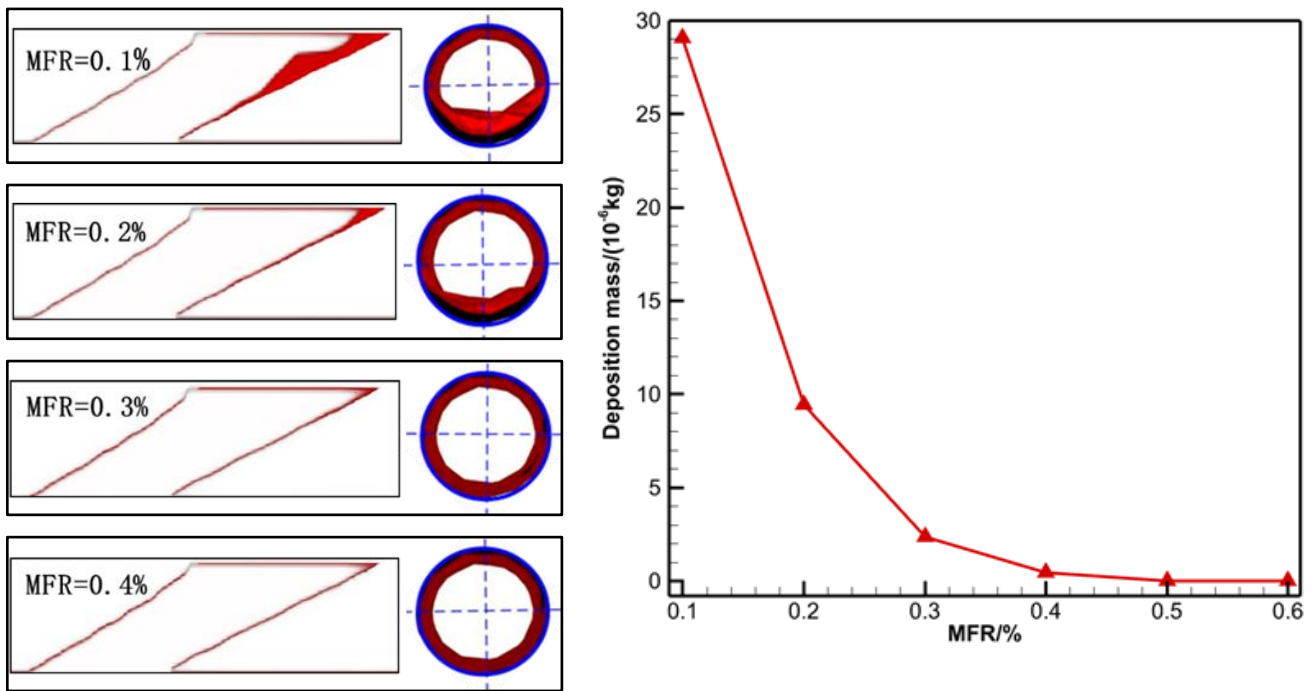
(a) Deposition morphology inside the film holes   (b) Deposition mass inside the film holes

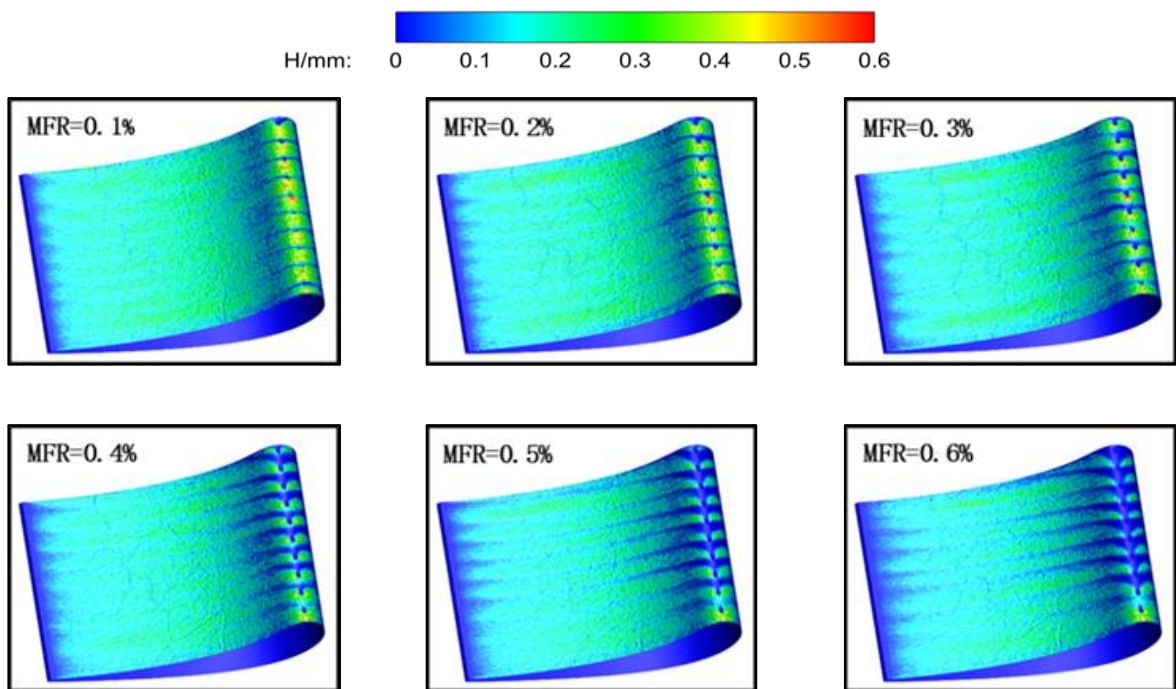**Fig. 5 Particle deposition inside the film holes**

Fig. 6 Deposition height on the blade

low wall temperature and the coolant flowing on the particles. At a low MFR (0.1%), the area covered by the film downstream of the film holes is small, resulting in a large deposition area. The non-deposition region extends slightly downstream of the film holes when the MFR increases to 0.2%-0.3%. At MFRs of 0.4%-0.6%, the wall temperature is lower, and the coolant has higher velocity, resulting in a wide and long non-deposition area downstream of the film holes.

Figure 7 shows the spanwise-averaged deposition height on the blade surface at different MFRs. The horizontal axis represents the ratio of the distance from the stagnation line on the leading edge to the hole diameter. Positive values indicate the ratio on the pressure surface, and negative values represent those on the suction surface. Negligible deposition occurs on the suction surface at s/d = -5. However, deposition occurs on the pressure surface at values larger than s/d=10. As the coolant dissipates, the
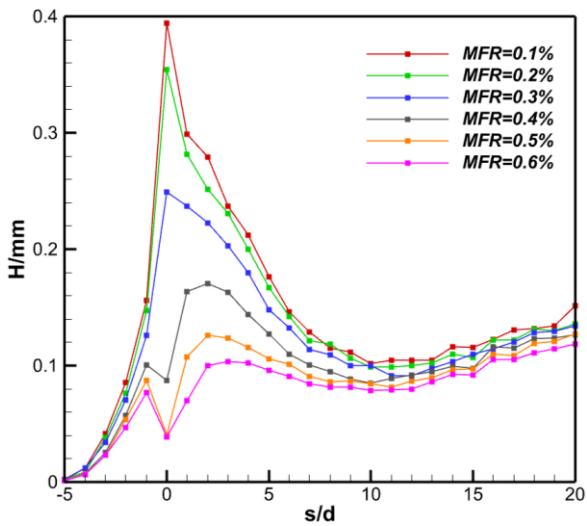
Fig. 7 Spanwise-averaged deposition height on the blade

difference in the effect of the coolant injection on the deposition between different MFRs becomes negligible, and the effect of the MFR on the deposition height is more pronounced near the film hole. At MFRs of 0.1%-0.3%, the spanwise-averaged deposition height is larger near the film holes than in other regions. The non-deposition area downstream of the hole extends gradually to the film holes as the MFR increases. At MFRs of 0.4%-0.6%, the

coolant's removal of the adhered particles causes less deposition near the film holes, resulting in smaller spanwise-averaged deposition heights.

As the MFR increases from 0.1% to 0.6%, the impact rates are similar, and the deposition rates decrease. An increase in the film-covered area and a decrease in the wall temperature reduce the adhesion rate. The increased wall friction velocity causes the detachment of particles from the wall due to the increased velocity of the coolant jet. Thus, a decrease in the adhesion rate and an increase in the detachment rate decrease the particle deposition rate.

4.2 Effect of Particle Deposition on Film Cooling Performance

The continuous phase flow field was calculated considering the updated boundary after deposition. The velocity field inside the film holes is shown in Fig. 8. The dashed line represents the wall surface without particle deposition, and the white region denotes the wall with particle deposition. At low MFRs of 0.1%-0.3%, a relatively large deposition amount inside the film holes increases the angle of the coolant jet, resulting in the strong separation of the film downstream of the film holes. At MFRs of 0.4%-0.6, the effect of deposition on the velocity field inside the film holes is weak due to a thin layer. The main reason for the decrease in film effectiveness after deposition is the limited spanwise diffusion of the coolant caused by the deposition morphology on the blade surface. This finding implies that
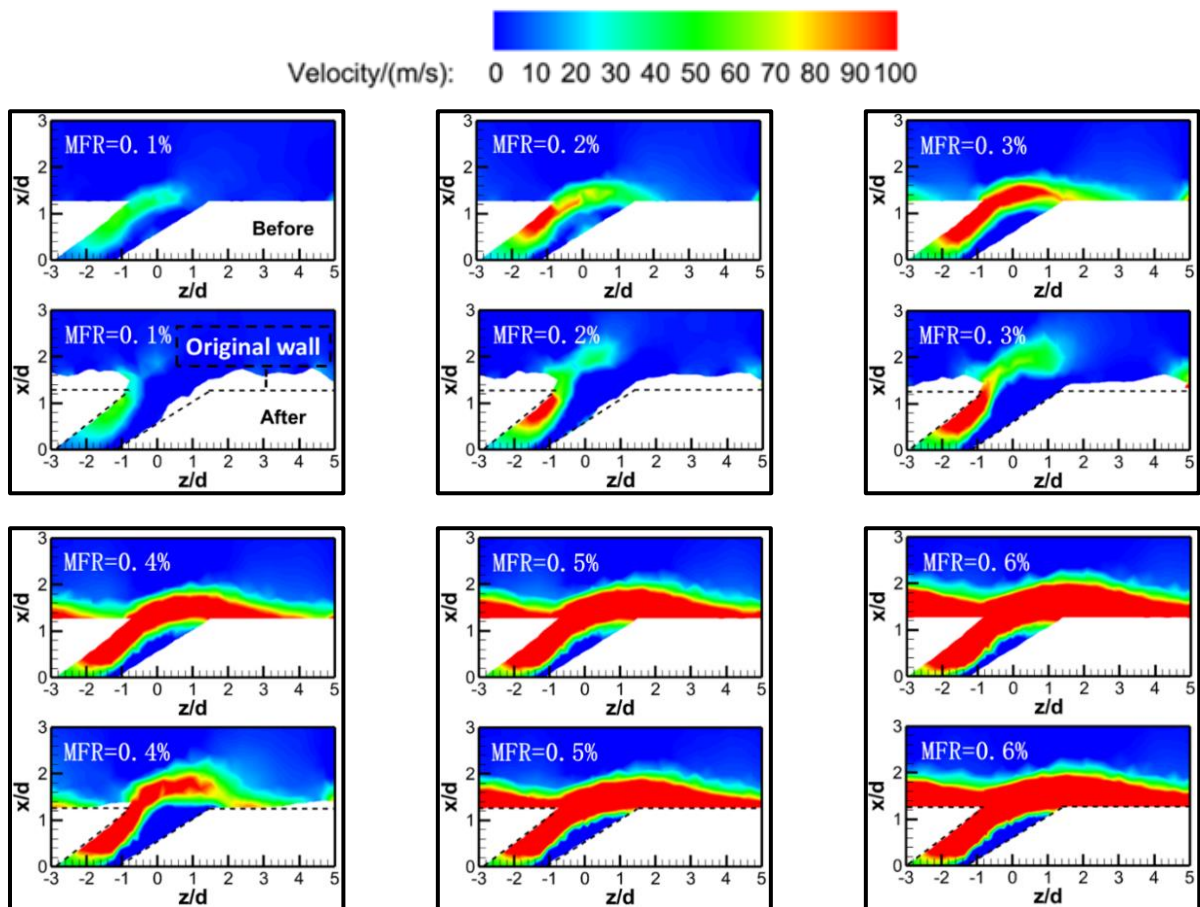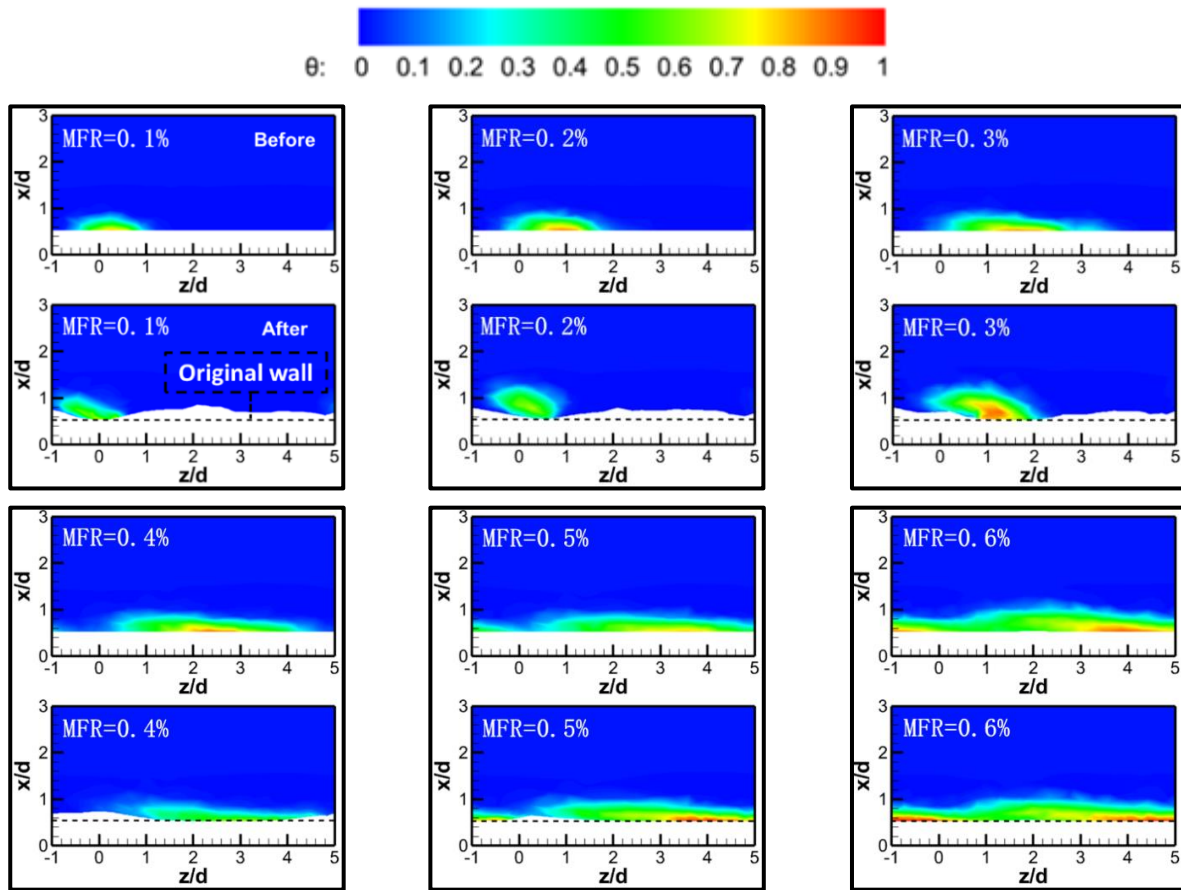

Fig. 8 Velocity field inside the film holes

Fig. 9 Dimensionless temperature distribution on the s/d=1 plane downstream of the film holes

the effect of the deposition on the spanwise diffusion of the coolant is greater inside the film hole than on the blade surface at low MFRs; the opposite occurs at higher MFRs.

Figure 9 shows the dimensionless temperature field on the s/d=1 plane downstream of the film hole for different MFRs. The spanwise region covered by the coolant gradually shifts to the positive z-direction (z is the spanwise direction) as the MFR increases. Since the increased jet momentum caused by the deposition inside the holes offsets the effect of the blade surface deposition amount on the spanwise diffusion of the coolant at low MFRs, no significant difference is observed in the spanwise coverage of the coolant before and after deposition. As the MFRs, the deposition amount near the film holes decreases, resulting in a negligible difference in film effectiveness before and after deposition at high MFRs.

Figure 10 shows the two-dimensional film effectiveness. At low MFRs, the increased coolant jet momentum is caused by the deposition effect on the blade, resulting in a minor difference in the film effectiveness before and after deposition. As the MFR increases, the deposition amount in the film hole decreases significantly, and the flow in the film hole is similar before and after deposition. However, the effect of the blade deposition on the spanwise diffusion of the coolant remains significant, reducing film effectiveness. At MFRs of 0.4% to 0.6%, the difference between the film effectiveness before and after deposition is small due to the small deposition amount.
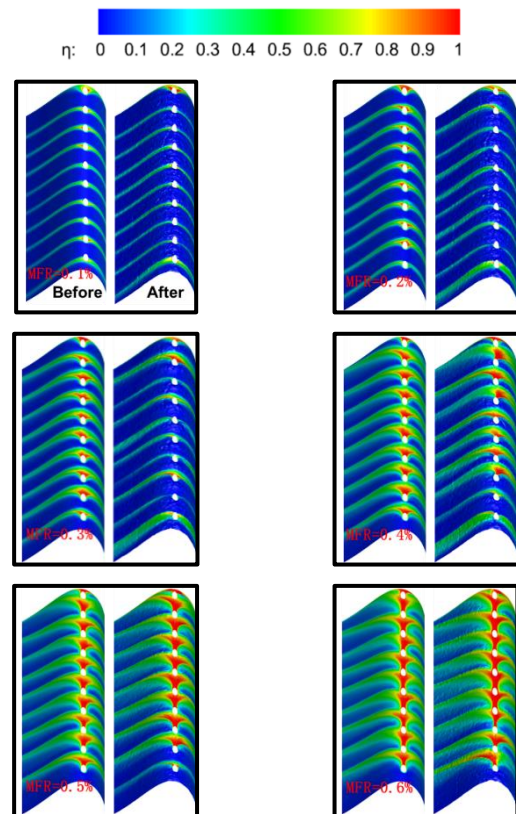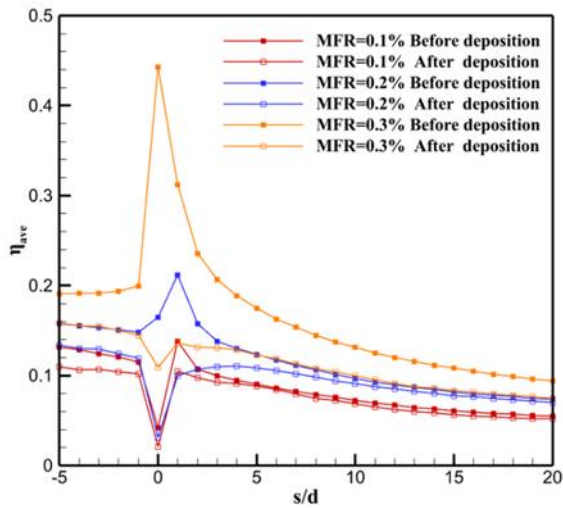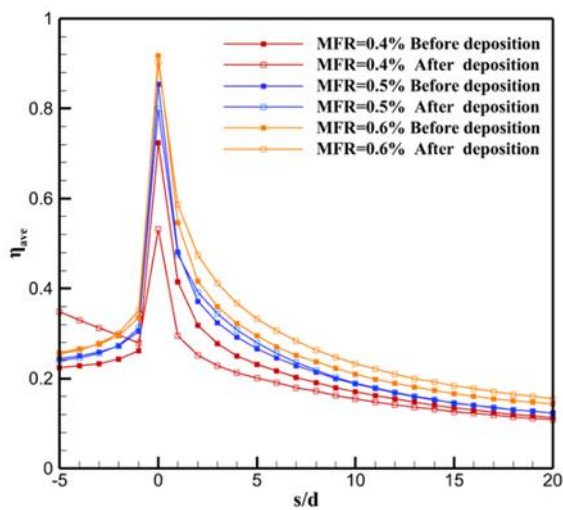

Fig. 10 Comparison of two-dimensional film effectiveness

(a) MFR=0.1%、0.2%、0.3%

(b) MFR=0.4%、0.5%、0.6%

Fig. 11 Comparison of spanwise-averaged film effectiveness before and after deposition

Figure 11 compares the spanwise-averaged film effectiveness before and after deposition. The effect of the deposition morphology on film effectiveness is in good agreement with the experimental results of Yang et al. (2021b). As the MFR increases, the spanwise-averaged film effectiveness near the holes increases significantly for the non-deposition and deposition cases. At MFRs of 0.1%-0.2%, the combined effect of the deposition inside the film holes and on the blade slightly changes the spanwise-averaged film effectiveness. The greatest reduction in the film effectiveness after deposition occurs at an MFR of 0.3%. At MFRs of 0.4%-0.5%, the reduction in film effectiveness after deposition is attributed to the smaller spanwise coverage area of the coolant. However, the deposition morphology is less pronounced, and the effect of the coolant is lower at higher MFRs, resulting in a smaller decrease in the film effectiveness after deposition. At an MFR of 0.6%, the film effectiveness is slightly higher after deposition.

Figure 12 shows the surface-averaged film effectiveness at different MFRs (area of $-5 \leq s/d \leq 20$ and
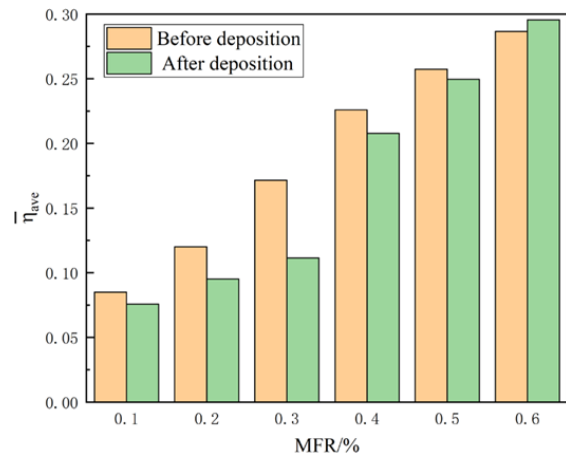

Fig. 12 Comparison of surface-averaged film effectiveness before and after deposition

$-29 \leq z/d \leq 29$). The surface-averaged film effectiveness after deposition is lower at MFRs of 0.1%-0.5% and slightly higher at an MFR of 0.6%. The particle deposition has the most significant influence on film effectiveness at an MFR of 0.3%. The film effectiveness is 34.9% lower after than before deposition.

5. CONCLUSION

The particle deposition distribution and the influence of the deposition morphology on the film cooling performance were numerically investigated using an improved composite deposition model and dynamic mesh updating at the operating temperature and pressure. Six MFRs were investigated. The conclusions were as follows:

1) A conical deposition formed inside the film hole at low MFRs. The deposition was negligible at MFRs exceeding 0.4%.

2) The particle deposition inside the hole and on the blade surface affected film effectiveness. The conical deposition enhanced the separation of the coolant from the wall inside the film hole at low MFRs. The effect of blade surface deposition on the velocity field after mixing between the mainstream and coolant was more significant than the effect of deposition inside the film hole as the MFR increased.

3) The deposition on both sides of the film-covered region restricted the coolant's spanwise diffusion, reducing the width of the area covered by the coolant. The surface-averaged film effectiveness was lower after deposition for MFRs of 0.1% to 0.5%. The most significant decrease in film effectiveness (34.9%) occurred at an MFR of 0.3%. The film effectiveness was slightly higher after than before deposition at an MFR of 0.6%.

4) More deposition inside the film holes occurred at low MFRs, and fewer particles were deposited at high MFRs. A high MFR on the leading edge of the blade reduced the effect of particle deposition on the film's cooling performance.

ACKNOWLEDGMENTS

CONFLICT OF INTEREST

The authors have no conflicts to disclose.

AUTHOR CONTRIBUTION

Guangchao Li: Funding acquisition, Writing-review & editing; **Guoji Zhang**: Writing-original draft; **Hongbin He**: Project administration; **Changyu Zhao**: Supervision, **Zhiqi Zhao**: Software; **Wei Zhang**: Validation.

REFERENCES

Abbasi, S., & Gholamalipour, A. (2020). Parametric study of injection from the casing in an axial turbine. *Proceedings of the Institution of Mechanical Engineers, Part A: Journal of Power and Energy*, *234*(5), 582-593. https://doi.org/10.1177/0957650919877276

Abbasi, S., & Gholamalipour, A. (2021). Performance optimization of an axial turbine with a casing injection based on response surface methodology. *Journal of the Brazilian Society of Mechanical Sciences and Engineering*, *43*(9), 435. https://doi.org/10.1007/s40430-021-03155-6

Ai, W., & Fletcher, T. H. (2012). Computational analysis of conjugate heat transfer and particulate deposition on a high pressure turbine vane. *ASME. J. Turbomach,* *134*(4), 041020. https://doi.org/10.1115/1.4003716

Ai, W., Murray, N., Fletcher, T. H., Harding, S., & Bons, J. P. (2011). Effect of hole spacing on deposition of fine coal flyash near film cooling holes. *Journal of Turbomachinery,* *134*(4), 041021. https://doi.org/10.1115/1.4003717

Albert, J. E., & Bogard, D. G. (2012). Experimental simulation of contaminant deposition on a film cooled turbine airfoil leading edge. *Journal of Turbomachinery,* *134*(5), 051014. https://doi.org/10.1115/1.4003964

Albert, J. E., & Bogard, D. G. (2013). Experimental simulation of contaminant deposition on a film-cooled turbine vane pressure side with a trench. *Journal of Turbomachinery, 135*(5), 051008. https://doi.org/10.1115/1.4007821

Barker, B., Casaday, B., Shankara, P., Ameri, A., & Bons, J. P. (2012). Coal ash deposition on nozzle guide vanes—part ii: computational modeling. *Journal of Turbomachinery*. https://doi.org/10.1115/1.4006399

Bonilla, C., Clum, C., Lawrence, M., Casaday, B., & Bons, J. P. (2013). *The effect of film cooling on nozzle guide vane deposition*. Proceedings of the ASME Turbo Expo 2013: Turbine Technical Conference and Exposition. Volume 3B: Heat Transfer. San Antonio, Texas, USA. June 3–7, 2013. V03BT13A043. ASME. https://doi.org/10.1115/GT2013-95081

Bonilla, C., Webb, J., Clum, C., Casaday, B., Brewer, E., & Bons, J. P. (2012). The effect of particle size and film cooling on nozzle guide vane deposition. *ASME. J. Eng. Gas Turbines Power, 134*(10), 101901. https://doi.org/10.1115/1.4007057

Bons, J. P. (2010). A Review of surface roughness effects in gas turbines. *Journal of Turbomachinery,* 132(2), 021004. https://doi.org/10.1115/1.3066315

Bons, J. P., Prenter, R., & Whitaker, S. (2017). A Simple physics-based model for particle rebound and deposition in turbomachinery. *Journal of Turbomachinery*, *139*(8), 081009. https://doi.org/10.1115/1.4035921

Borello, D, Capobianchi, P, De Petris, M, Rispoli, F, & Venturini, P. (2014). *Unsteady RANS analysis of particles deposition in the coolant channel of a gas turbine blade using a non-linear model*. Proceedings of the ASME Turbo Expo 2014: Turbine Technical Conference and Exposition. Volume 5A: Heat Transfer. Düsseldorf, Germany. June 16–20, 2014. V05AT12A035. ASME. https://doi.org/10.1115/GT2014-26252

Brach, R. M., & Dunn, P. F. (1992). A mathematical model of the impact and adhesion of microspheres. *Aerosol Science and Technology*, *16*(1), 51-64. https://doi.org/10.1080/02786829208959537

Crosby, J. M., Lewis, S., Bons, J. P., Ai, W., & Fletcher, T. H. (2008). Effects of temperature and particle size on deposition in land based turbines. *Journal of Engineering for Gas Turbines & Power*, *130*(5), 819-825. https://doi.org/10.1115/1.290390

Dunn, M. G. (2012). Operation of gas turbine engines in an environment contaminated with volcanic ash. *Journal of Turbomachinery*, *134*(5), 051001. https://doi.org/10.1115/1.4006236

El-Batsh, H., & Haselbacher, H. (2002) *Numerical investigation of the effect of ash particle deposition on the flow field through turbine cascades.* Proceedings of the ASME Turbo Expo 2002: Power for Land, Sea, and Air. Volume 5: Turbo Expo 2002, Parts A and B. Amsterdam, The Netherlands. June 3–6, 2002. pp. 1035-1043. ASME. https://doi.org/10.1115/GT2002-30600

Hao, Z., Yang, X., & Feng, Z. (2023). Unsteady modeling of particle deposition effects on aerodynamics and heat transfer in turbine stator passages with mesh morphing. *International Journal of Thermal Sciences*, 190, 108326. https://doi.org/10.1016/j.ijthermalsci.2023.108326

https://doi.org/10.1115/GT2010-22376

Jensen, J. W., Squire, S. W., Bons, J. P., & Fletcher, T. H.

(2004). Simulated land-based turbine deposits generated in an accelerated deposition facility. *Journal of Turbomachinery*, *127*(3), 462–470. https://doi.org/10.1115/1.1860380

Kim, J., Dunn, M. G., Baran, A. J., Wade, D. P., & Tremba, E. L. (1993). Deposition of volcanic materials in the hot sections of two gas turbine engines. *Journal of Engineering for Gas Turbines and Power,* *115*(3), 641–651. https://doi.org/10.1115/1.2906754

Kistenmacher, D. A., Davidson, F. T., & Bogard, D. G. (2013). Realistic trench film cooling with a thermal barrier coating and deposition. *American Society of Mechanical Engineers,* *(9)*. https://doi.org/10.1115/1.4026613

Lawson, S. A., & Thole, K. A. (2010, October). *Simulations of multi-phase particle deposition on endwall film-cooling.* Turbo Expo: Power for Land, Sea, and Air. (Vol. 43994, pp. 151-162). https://doi.org/10.1115/GT2010-22376

Lawson, S. A., & Thole, K. A. (2011). Effects of simulated particle deposition on film cooling. *Journal of Turbomachinery,* *133*(2), 41-51. https://doi.org/10.1115/GT2009-59109

Lawson, S. A., Thole, K. A., Okita, Y., & Nakamata, C. (2012). Simulations of multiphase particle deposition on a showerhead with staggered film-cooling holes. *Journal of Turbomachinery, 134*(5), 051041. https://doi.org/10.1115/1.4004757

Lewis, S., Barker, B., Bons, J. P., Ai, W., & Fletcher, T. H. (2010). Film cooling effectiveness and heat transfer near deposit-laden film holes. *Journal of Turbomachinery,* *133*(3), 031003. https://doi.org/10.1115/1.4001190

Lee, S., Hwang, W., & Yee, K. (2018). Robust design optimization of a turbine blade film cooling hole affected by roughness and blockage. *International Journal of Thermal Sciences,* 133, 216-229.

Liu, C. L., Xie, G., Wang, R., & Ye, L. (2018). Study on analogy principle of overall cooling effectiveness for composite cooling structures with impingement and effusion. *International Journal of Heat and Mass Transfer*, *127* (PT.B), 639-650. https://doi.org/10.1016/j.ijheatmasstransfer.2018.07.085

Lundgreen, R., Sacco, C., Prenter, R., & Bons, J. P. (2016). *Temperature effects on nozzle guide vane deposition in a new turbine cascade rig.* Turbo Expo: Power for Land, Sea, and Air (Vol. 49781, p. V05AT13A021). American Society of Mechanical Engineers. https://doi.org/10.1115/GT2016-57560

Maikell, J., Bogard, D., Piggush, J., & Kohli, A. (2011). Experimental simulation of a film cooled turbine blade leading edge including thermal barrier coating effects. *Lewis* *133*(1), 011014. https://doi.org/10.1115/1.4000537

Senior, C. L., & Srinivasachar, S. (1995). Viscosity of ash particles in combustion systems for prediction of particle sticking. *Energy & Fuels*, 9(2), 277-283. https://doi.org/10.1021/ef00050a010

Sreedharan, S. S., & Tafti, D. K. (2011). Composition dependent model for the prediction of syngas ash deposition in turbine gas hotpath. *International journal of heat and fluid flow,* 32(1), 201-211. https://doi.org/10.1016/j.ijheatfluidflow.2010.10.006.

Sundaram, N., Barringer, M. D., & Thole, K. A. (2008). Effects of deposits on film cooling of a vane endwall along the pressure side. *Journal of Turbomachinery*, *130*(4), 786-791. https://doi.org/10.1115/1.2812332

Vali, S. E., & Abbasi, S. (2022). Hypersonic drag and heat reduction mechanism of a new hybrid method of spike, multi-row discs and opposing jets aerodynamic configuration. *International Journal of Heat and Mass Transfer*, *194*, 123034. https://doi.org/10.1016/j.ijheatmasstransfer.2022.123034

Vali, S. E., & Abbasi, S. (2024). Heat and drag reduction on the hypersonic nose with a nexus between active and passive control methods. *Physics of Fluids*, *36*(1). https://doi.org/10.1063/5.0176555

Wang, J., Cui, P., Sundén, Bengt, & Vujanovi, M. (2016). Effects of deposition height and width on film cooling. *Numerical Heat Transfer, Part A: Applications*, 1-15. https://doi.org/10.1080/10407782.2016.1193351

Yang, X., Hao, Z., Feng, Z. (2021a). Variations of cooling performance on turbine vanes due to incipient particle deposition. *Proceedings of the Institution of Mechanical Engineers, Part A: Journal of Power and Energy,* *235*(8), 1832-1846. https://doi.org/10.1177/09576509211010530

Yang, X., Hao, Z., & Feng, Z. (2021b). An experimental study on turbine vane Leading-Edge film cooling with deposition. *Applied Thermal Engineering, 198*, 117447. https://doi.org/10.1016/j.applthermaleng.2021.117447

Zhang, F., Liu, Z., Liu, Z., & Diao, W. (2020). Experimental study of sand particle deposition on a film-cooled turbine blade at different gas temperatures and angles of attack. *Energies*, *13*(4), 811. https://doi.org/10.3390/en13040811